Plasma Sources Sci. Technol. **8** (1999) 313–324. Printed in the UK PII: S0963-0252(99)02822-4

Hysteresis and the E-to-H transition in radiofrequency inductive discharges

M M Turner† and M A Lieberman‡

† Plasma Research Laboratory, School of Physical Sciences, Dublin City University, Ireland
‡ Department of Electrical Engineering and Computer Sciences, University of California, Berkeley, CA 94720, USA

Received 19 October 1998, in final form 15 March 1999

Abstract. Typical inductive discharges, such as are used for plasma processing, exhibit two modes of operation: the true inductive discharge known as the H mode, and a weak capacitive discharge known as the E mode. Experimentally, the transition between these modes as the coil current is increased is clear and is marked by a large increase in discharge power, plasma density and optical emission occurring as the H mode appears. According to simple theory, this transition and the reverse transition occur at a single well defined current. In practice, this is usually not the case. The E-to-H transition occurs at a larger coil current than the H-to-E transition, and a range of currents between these values supports either E or H mode. This effect is called hysteresis. In this paper we show that hysteresis can be understood to arise from nonlinear effects, most notably in the electron power balance equation. We survey various mechanisms that can produce hysteresis and attempt to provide quantitative estimates of their significance.

1. Introduction

Inductive discharges have been investigated scientifically almost continuously since their discovery in the last century. These studies have been motivated as often by economic imperatives as by abstract scientific curiosity, as a series of important applications of inductive discharges have been developed [1]. The operating conditions for these applications vary widely, especially with respect to discharge gas pressure, which can range from mTorrs or even less to atmospheric pressure or greater. The lower part of this pressure range, from a few mTorr to a few hundred mTorr, is widely used for semiconductor processing applications [2–4]. Inductive discharges operated at such low pressures present special theoretical problems, because the length and time scales usually considered microscopic, such as the mean free paths of electrons and ions, and the respective collision frequencies of these species, can be comparable with or even larger than the macroscopic scales of the discharges, such as their characteristic spatial dimensions and the period of the driving frequency.

Although much recent work has focused on these issues, they are not the only points of interest. This paper is concerned with another striking feature of this type of discharge, namely the existence of a threshold value of the radio frequency current exciting the discharge below which no inductive discharge can be formed. One can indeed form a discharge when the current is below this threshold, but this is a weak discharge of low density, dissipating comparatively little power, which is generally attributed to stray electrostatic coupling from the induction coil through which the radio frequency current passes. Thus an 'inductive' discharge supports two operating modes, the true inductive discharge, known as the H mode, which is an electromagnetic phenomenon, and an electrostatic or capacitive discharge, which is called the E mode. The existence of these two modes was recognized long ago, and was then an important discovery, since a notorious controversy concerning the operating mechanism of 'inductive' discharges was thereby resolved [5–8]. Theoretical arguments based on discharge power balance [3, 9–11], which we review below, make it clear why the threshold current exists. However, scrutiny of recent [9, 12] and older experiments [13] demonstrates that the threshold current is not in fact always so well defined: there is usually a difference between the minimum coil current required to initiate the inductive discharge (the starting current) and the minimum coil current required to sustain the inductive discharge once it is formed (the maintenance current). Consequently, a range of coil currents exists that can support either an E or an H mode discharge, with the mode actually present depending on the history of the system. Such behaviour is called *hysteresis*.

In this paper we show how power balance arguments may be extended to admit hysteresis. In section 2 we outline the arguments that lead to the expectation of a threshold current for ideal H mode discharge operation. In section 3 we identify sundry mechanisms omitted from the ideal model of section 2 that may produce hysteresis and discuss their relative importance in typical circumstances. These mechanisms are related to nonlinearities in the plasma itself or in its interaction with the coil. Finally in section 4 we show how the presence of hysteresis can change the characteristics of inductive discharge systems coupled to non-ideal excitation circuits, and in particular we show that

0963-0252/99/020313+12$19.50

hysteresis is affected by the configuration of, e.g., matching networks.

2. Background theory

Any plasma discharge has to satisfy two basic equilibrium conditions, namely particle balance and power balance [3, 14]. The combination of these constraints essentially explains the mode transitions that are observed in inductive discharges, as we will show. In an electropositive plasma under the conditions we are considering, particles are created in the plasma volume by electron impact ionization and recombine at the walls. Therefore the particle balance condition is that the volume integral of the ionization source term S must equal the surface integral of the flux F of charged particles to the wall:

$$\int_V S \, \mathrm{d}V = \int_S F \, \mathrm{d}A. \tag{1}$$

If we assume that the plasma density and electron temperature are uniform or can be represented by volume averages, then this equation determines the electron temperature, since both sides are proportional to the plasma density and there are no other unknowns.

If the electron temperature is fixed, then the energy that must be supplied to support an electron–ion pair over its lifetime is also fixed, and the plasma density is proportional to the power dissipated by the discharge electrons:

$$n = \frac{P_{dis}}{u_B A_{eff} \epsilon_{T_e}} \tag{2}$$

in the notation of [3], where n is the plasma density, P_{dis} is the power dissipated by the electrons, u_B is the Bohm velocity, A_{eff} is the effective surface area of the plasma and ϵ_{T_e} is the electron energy lost per electron–ion pair created in the discharge. This energy loss is primarily due to electron–neutral elastic and inelastic collisional processes (ionization, excitation etc). For rare gases, where basic data such as cross sections are available, the quantities appearing in this expression can be calculated with fair accuracy for simple geometries and low pressures. For higher pressures, and more complex gases and geometries, such computation may be impractical, but it is sometimes reasonable to assume nevertheless that a constant of proportionality exists between power and plasma density, as experiments and simulations generally show.

The power P_{dis} that is required to sustain the discharge at any given density must be supplied by the external circuit, in this case the induction coil. It is convenient to characterize the response of the plasma to the currents flowing in the induction coil in terms of a surface impedance (which has the same dimensions as ordinary impedance, i.e., Ω) given by

$$\zeta \equiv \frac{E}{\mathcal{J}} \tag{3}$$

where E is the complex amplitude of the rf electric field at the surface of the plasma and $\mathcal{J}$ is the rf amplitude of the surface current (here taken to be purely real, with units of A m^{-1}). These quantities are related by geometrical factors

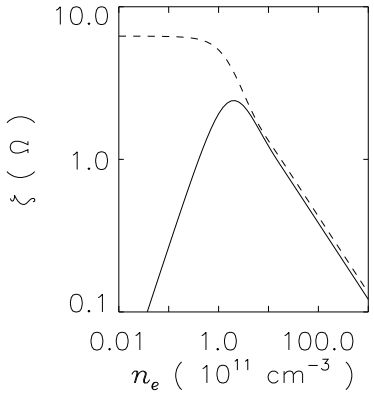

Figure 1. The surface impedance of an inductive discharge plasma as a function of electron density, showing the imaginary part (dashed line) as a monotonically decreasing function of the electron density and the real part (solid line) having a peak where the skin depth is comparable with the chamber size. This example calculation is for a plasma slab of thickness 6 cm and ratio of electron collision frequency to angular driving frequency $\nu/\omega_{rf} = 10$.

to the voltage across the coil and the coil current, and the real and imaginary parts of ζ are correspondingly related to the resistance R_L and coil inductance L_L of the more general model discussed below. If the electron temperature is independent of the plasma density, then so is the electron collision frequency (supposing electron–neutral collisions to be dominant), and in such a case the surface impedance is a function of the electron density. The variation of the surface impedance with electron density can be calculated analytically in simple geometries: For a one dimensional plasma slab of thickness L it is given by [15, 16]

$$\zeta = \frac{\mathrm{i}\omega\mu_0}{k} \tanh kL \tag{4}$$

where $k = (\omega_p/\sqrt{2}c)[\sqrt{\phi(1+\phi)} + \mathrm{i}\sqrt{\phi(1-\phi)}]$, ω_p is the electron plasma frequency and $\phi = 1/\sqrt{1+\nu_e^2/\omega^2}$ with ν_e the electron–neutral collision frequency. Figure 1 shows the real and imaginary parts of this expression as functions of the electron density. The behaviour shown here is qualitatively the same in any geometry. Of special interest is the real part, since the power dissipated in the plasma by its interaction with the coil is given by

$$P_{abs} = \tfrac{1}{2} A_{plasma} \, \mathrm{Re}\, \zeta \mathcal{J}^2 \tag{5}$$

where A_{plasma} is the surface area over which the plasma is excited. Note that as figure 1 shows, for small electron densities the real part of the surface impedance is proportional to the electron density. In this regime the skin depth is much larger than the system size. At higher electron densities the skin effect begins to exclude the induced electric field from the plasma, and the real part of the surface impedance decreases. The peak of the real part of the surface impedance occurs when the skin depth is comparable with the size of the chamber.

Electron power balance requires that P_{abs} in equation (5) be identical with P_{dis} appearing in equation (2); i.e.,

$$\frac{1}{2} A_{plasma} \, \mathrm{Re}\, \zeta(n) \mathcal{J}^2 = \frac{n}{u_B A_{eff} \epsilon_{T_e}}. \tag{6}$$

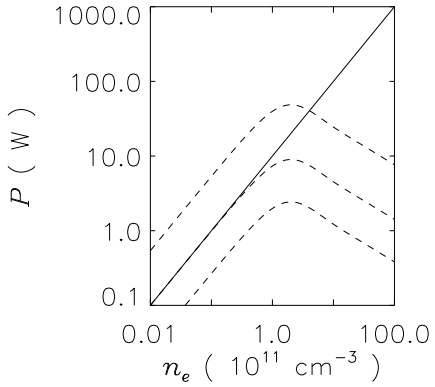

Figure 2. Power balance diagrams for an ideal inductive discharge without capacitive coupling or hysteresis effects, showing the appearance of a stable operating point when the coil current exceeds some threshold. The solid line is the fixed curve of P_{dis} as a function of n, while the dashed curves show P_{abs} for three values of the coil current: less than the starting current equal to the starting current; and greater than the starting current. In all cases there is an equilibrium point at $n = 0$ which is not shown in this diagram. This equilibrium point is unstable once the threshold current is exceeded.

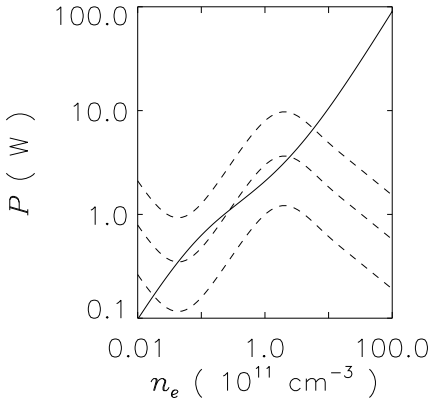

Figure 3. A power balance diagram for the electrons in a non-ideal inductive discharge including capacitive coupling and nonlinear ionization processes leading to hysteresis. As in figure 2, the solid line is the fixed curve of P_{dis} as a function of n, while the dashed curves show P_{abs} for three values of the coil current. The upturn in these curves at the left-hand side of the figure is due to dissipation in the capacitive branch of the equivalent circuit shown in figure 4, which is important at low electron density. The family of curves of P_{abs} all have $P_{abs} = 0$ at $n = 0$, so there exists some finite starting current for the E mode which is not shown here [37]. The lower dashed curve is below the maintenance current for the H mode, with the single crossing point being a stable equilibrium corresponding to the E mode; the middle curve is between the maintenance current and the starting current—here two stable operating points corresponding to the E and H modes are separated by an unstable equilibrium point; the upper curve is above the starting current and the single crossing point is an H mode equilibrium.

This is an equation for the plasma density, that might also be written as

$$\frac{1}{2}R_L I^2 = \frac{n}{u_B A_{eff} \epsilon_{T_e}} \tag{7}$$

where I is the coil current and R_L is the resistance presented to the coil by plasma electrons. These equations have either one or two solutions depending on the value of $\mathcal{J}$, as shown in figure 2. If there is only one solution, it is at $n = 0$; if there are two solutions, one is at $n = 0$ and the second is at some finite density, and since the first of these solutions is always unstable with respect to the second, the finite density solution is the physically relevant one. This argument indicates that a pure inductive discharge exists only when I exceeds some well defined threshold. At small enough electron densities, R_L is proportional to n and equation (7) can be written as

$$\frac{1}{2}\frac{\mathrm{d}R_L}{\mathrm{d}n} n I^2 = \frac{n}{u_B A_{eff} \epsilon_{T_e}} \tag{8}$$

so that the smallest current that will maintain the inductive discharge is

$$I_m = \left(\frac{2}{(\mathrm{d}R_L/\mathrm{d}n) u_B A_{eff} \epsilon_{T_e}} \right)^{1/2}. \tag{9}$$

As we suggested in section 1, this is too simple a picture, and we now proceed to consider how things must change to accommodate hysteresis effects.

3. Mechanisms producing hysteresis

The appearance of hysteresis implies the existence of more than one stable equilibrium of equation (7), the power balance equation, for a given value of the coil current. This can happen if either P_{abs} or P_{dis} or both depart from the linear behaviour assumed in equation (9). Such nonlinearities can be divided into circuit or absorbed power nonlinearities, affecting the left-hand side of equation (8), and plasma or dissipated power nonlinearities, affecting the right-hand side. When nonlinearity of this type is present, there can be one or two stable operating points with $n \neq 0$, corresponding to E mode only, H mode only, or the possibility of either. Examples are shown in figure 3, for the case where the nonlinearity is in P_{dis}.

In the two subsections following we discuss various mechanisms that tend to produce nonlinearities that might be responsible for hysteresis effects. We attempt to quantify the size of the effects, and thus assess their likely significance in typical experiments. Our calculations are predominantly analytic, but we have made use of a kinetic plasma simulation code based on the particle in cell algorithm with Monte Carlo collisions [17, 18]. This simulation is one dimensional and has cylindrical geometry, with the radial coordinate explicitly represented. Both particles and fields are advanced in time using an implicit procedure [19], so that none of the usual stability conditions relating to plasma frequency, Debye length and the transit time of light waves applies. Consequently, this code can simulate discharges with electron density 10^{12} cm^{-3} or higher, with computer resources no greater than are required for simulations of capacitive discharges of two or three orders of magnitude less density. A wider range of collision processes than usual is also represented, so that the significance of Coulomb collisions [20] and other nonlinear processes to be discussed below can be assessed.

3.1. Nonlinearities in absorbed power

3.1.1. General remarks. From a strictly electrical perspective, the most important difference between a real inductive discharge and the idealized model discussed above is that some of the discharge power will always be deposited capacitively in a real discharge: there will necessarily be a substantial voltage produced across the induction coil, and this voltage will drive a capacitive current in the plasma. The nonlinearities to be discussed in this section are all related to the presence of this capacitive effect. Such stray capacitive coupling is responsible for the E mode discharge discussed above. The effect can be made small by the introduction of, e.g., a Faraday shield, but this measure is not completely effective, and is not commonly adopted in industrial practice because it reduces the inductive coupling efficiency.

In a real discharge the capacitive current distributes itself across the antenna in a fashion that is complex to evaluate without a full multi-dimensional treatment. For analytic purposes it is convenient to represent the inductive discharge with capacitive coupling by a lumped element circuit model, as has often been adopted before [21, 22], and as shown in figure 4. In the present case there are two parallel branches representing the current paths through the antenna (the inductive branch) and through the dielectric window (the capacitive branch). The rf voltage V_{rf} is the same for each path. Capacitive coupling is modelled by the series combination of the coil-to-plasma window capacitance C_q, the sheath capacitance C_c and the resistors R_{ohm} and R_{ion}, representing respectively the capacitive energy deposited into the discharge electrons due to ohmic heating and the heating of ions that fall through the dc sheath potential $V_{dc} \approx 0.4V_c$, where V_c is the rf voltage magnitude across the sheath. The ion resistance represents the energy supplied by the rf source to maintain the sheath against the flow of ions to the wall. This sometimes important contribution to the total discharge power balance is not included in equation (6), which represents the electron power balance only. The inductive coupling is represented as a transformer having primary inductance L_1 and winding resistance R_1, secondary (geometric) inductance L_2 and mutual inductance M, with the secondary connected to a series combination of the electron inertia inductance L_e and the plasma resistance R_e. L_e and R_e give the reactive and resistive response of the one turn plasma loop to the induced secondary voltage generated by the rf inductive electric field. Figure 4 also shows details of the matching network, which will be addressed in section 4 below. It is customary to transform the secondary load into the primary circuit of the transformer, as shown in the figure. Here

$$L_L = L_1 - \frac{\omega^2 M^2 (L_2 + L_e)}{R_e^2 + \omega^2 (L_2 + L_e)^2} \tag{10}$$

$$R_L = R_1 + \frac{\omega^2 M^2 R_e}{R_e^2 + \omega^2 (L_2 + L_e)^2}. \tag{11}$$

The capacitive and inductive circuits in figure 4 are in parallel and would seem to respond independently to a given antenna voltage V_{rf}. However, these circuits are coupled because the plasma-dependent lumped element values are not constant but are nonlinear functions of the plasma density and the sheath voltage.

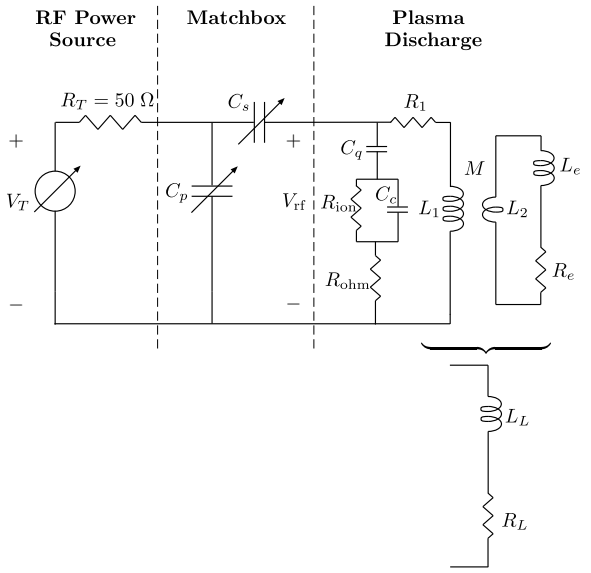

Figure 4. Lumped element models: (above) basic model with capacitive and transformer coupled inductive circuit; (below) with the secondary transformer impedance transformed into the primary circuit.

In principle, the circuit-related nonlinearities that we discuss in this section can be experimentally distinguished from the plasma nonlinearities to be discussed in section 3.2 below, since all the circuit effects are associated with capacitive currents, and these can be at least partially suppressed by Faraday shielding. The plasma nonlinearities, however, should not be so affected.

3.1.2. Dependence of the reactances on plasma density. A nonlinear behaviour for P_{abs} in the left-hand term of equation (9) can arise simply because the partition of current between the inductive and capacitive branches depends on the plasma density. For typical values of the circuit parameters, the branch impedances are mostly reactive (i.e. the real part of the impedance is relatively small) and both of the branch impedances have a component that depends on the plasma density, since the capacitance branch includes the capacitance of the plasma sheath adjacent to the coil, and the inductance of the coil is partly modified by the coupling to the plasma as shown in figure 1.

3.1.3. Child law sheath capacitance. At high voltages, $V_c \gg T_e$, the sheath has a Child law behaviour with a sheath capacitance $C_c = KV_c^{-3/4}$. Here V_c (a positive real number) is the amplitude of the rf voltage across the sheath and K is a constant of proportionality. If we ignore the resistive components, then depending on the settings of the matching network elements, window capacitance and plasma parameters, the sheath capacitance can 'see' (be driven by) an inductive Thevenin-equivalent source with some positive real amplitude V and source impedance jX (X is a positive real reactance). Equating the rf current supplied by this source to the current I flowing through the sheath, we obtain

$$\frac{V_c \pm V}{X} = \omega C_c V_c = \omega K V_c^{1/4} \tag{12}$$

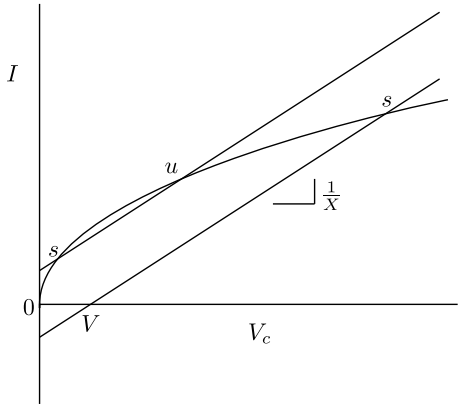

Figure 5. Sheath current amplitude I versus sheath voltage amplitude V_c, at a fixed Thevenin-equivalent source voltage amplitude V; the curve is the I–V_c characteristic of the Child law sheath capacitance, and the two straight lines are the out-of-phase (top) and in-phase (bottom) Thevenin source characteristics; s and u denote stable and unstable solutions.

where the $\pm$ signs correspond to the voltages V_c and V either being 180° out of phase or in phase, respectively. As illustrated in figure 5, for $V < 3(\omega X K/4)^{4/3}$, there are two stable solutions for V_c (one with V and V_c in phase, and one out of phase), yielding a hysteresis in the discharge (V–I) characteristic. It can be shown that the resistive components modify but do not destroy this potential source of hysteresis.

3.1.4. Paschen sheath breakdown. At high pressures and/or sheath voltages the mean free path for creation of electron–ion pairs within the sheath can be equal to or smaller than the sheath thickness, leading to breakdown of the sheath. In this case the discharge can make an abrupt transition from the so-called α regime, where ionization in the plasma bulk sustains the discharge, to the so-called γ regime, where the multiplication of secondary electrons emitted by the electrodes as a result of ion bombardment plays a very important role in discharge maintenance [23]. This form of rf discharge is similar to a dc glow discharge in that the electrodes behave as 'cathodes' during part of the rf cycle. The sheath thickness is usually much smaller than the sheath of an α discharge, while the ion density and electric field in the sheath are larger.

The condition for formation of a γ discharge is very similar to the condition for breakdown of a gap between two plane electrodes in a low pressure gas, the so-called *Paschen breakdown*, with the maximum sheath width and maximum voltage playing the role of the gap width and the dc Paschen breakdown voltage. A simple analytical evaluation of the transition from the α to the γ regime is given in Raizer *et al* [24], based on this analogy. Adapting such a model, we can introduce an approximate form for the breakdown curve:

$$V_c = V_p + \Delta V_p \left(\log \frac{p s_\gamma}{(pd)_{min}} \right)^2 \qquad (13)$$

where s_γ is the sheath width in the γ regime, $V_p \approx 140$ V, $\Delta V_p \approx 34.8$ V, and $(pd)_{min} \approx 0.003$ Torr m for argon. Ignoring the resistive elements, the capacitive

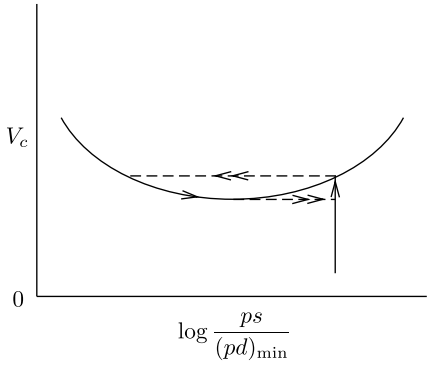

Figure 6. Sheath voltage V_c versus sheath thickness s; the solid curve gives the breakdown characteristics of the sheath; the hysteresis loop is shown with arrows.

voltage division across the quartz window and sheath yields the expression:

$$V_c = 0.83 V_{rf} \left(1 + \frac{C_c}{C_q} \right)^{-1} \qquad (14)$$

where $C_c \propto s_\gamma^{-1}$. Equating (13) and (14) for a given coil voltage V_{rf}, we can solve for s_γ.

For $V_c > V_p$, the breakdown curve equation (13) has two solutions for s_γ at a given V_c. This can be a source of hysteresis. If the Child law sheath thickness $s_m > s_\gamma$, then the discharge enters the γ regime. Analogous to the abnormal regime of a dc glow discharge, for $ps < (pd)_{min}$, this transition is continuous, with a continuously increasing V_c yielding a continuously decreasing sheath thickness $s = s_\gamma(V_c)$ after the γ regime has been entered. However, for $ps > (pd)_{min}$, an abrupt transition to a smaller sheath width with $ps < (pd)_{min}$ (higher plasma density in the sheath) is possible, as has been observed [23]. First increasing and then decreasing V_c can then lead to a hysteresis loop as illustrated in figure 6.

3.1.5. Reduced inductive coupling due to capacitive sheath. It is evident that the existence of capacitive coupling will lead to the appearance of a capacitive sheath in the region between the coil and the plasma. A driven sheath of this kind is substantially wider than an undriven Bohm sheath, so one effect of the presence of capacitive coupling is to substantially exclude the plasma from a region adjacent to the coil; i.e., to decrease the electron density from n to $\bar{n}$ near the coil. This effect can also be thought of as equivalent to increasing the effective thickness of the dielectric window separating the coil and the plasma, which generally has the effect of reducing the effectiveness of inductive coupling (decreasing the mutual inductance M). As the width of the capacitive sheath is substantially less in the high density H mode relative to the low density E mode, inductive coupling is somewhat suppressed in the E mode, and this can have the effect of postponing the transition to H mode to higher coil currents that would otherwise be the case. Particle in cell calculations illustrating this effect are shown in figure 7.

A qualitative estimate of this effect, based on the condition of constant ion flux within a Child law sheath, is

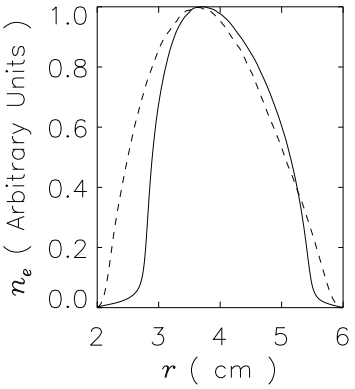

Figure 7. Particle in cell calculations illustrating how the capacitive sheath in a low density discharge interferes with inductive coupling and reduces its efficiency. The dashed line shows the inductive discharge density profile with a peak density $n \sim 10^{12}$ cm^{-3} and a thin sheath. The solid line is a capacitive discharge density profile with peak density $n \sim 10^{10}$ cm^{-3}. These data are selected from the calculations summarized in figure 10, further details of which are discussed in the text.

that $\bar{n} \propto n(T_e/V_c)^{1/2}$. A more accurate calculation, based on a self-consistent capacitive sheath model for $V_c \gg T_e$, is [25]

$$\frac{\bar{n}}{n} \approx 0.196\left(\frac{T_e\delta_p}{V_c s_m}\right)^{1/2} + \mathrm{e}^{-2s_m/\delta_p} \qquad (15)$$

where δ_p is the skin depth and s_m is the sheath thickness. Because R_e and L_e in figure 4 depend inversely on density within the skin depth layer, the result is a reduced inductive electron power absorption. This has been observed to lead to a significant hysteresis in some inductive discharges [12, 25].

3.1.6. Further remarks. To a large extent, the potential hysteresis due to the nonlinear sheath behaviour is buffered by the weak electrostatic coupling of the coil to the plasma, represented in figure 4 by a small window capacitance C_q. For representative values of the parameters, the fraction of the total current that flows through the capacitive branch while in H mode is generally less than 0.1, and capacitive current variations are insufficient to produce hysteresis effects of the magnitude observed in some experiments [12].

3.2. Nonlinearities in dissipated power

3.2.1. General remarks. In the electron power balance equation (6) and the succeeding development in section 2, the efficiency of plasma production is specified by ϵ_{T_e}, the electron energy that must be supplied to support an electron–ion pair over its lifetime. In section 2, this quantity was taken to be independent of the plasma density, but there are volume collisional processes that tend to violate this assumption: for example, Coulomb collisions between electrons, which make the electron energy distribution function (EEDF) more Maxwellian; and multi-step ionization through intermediate excited states of the background gas, which is a well known effect in, e.g., mercury discharges [26]. These processes tend to increase the proportion of the power absorbed by the electrons from the coil that directly produces ionization, and this is potentially a significant source of hysteresis, since direct ionization can be a rather small part of the power balance: the most important contribution to ϵ_{T_e} is the energy dissipated by electrons in elastic and inelastic collisions, ϵ_c, which in argon is ∼40–100 eV [3] and is considerably larger than the ionization energy of 15.8 eV, with the balance of the energy primarily deposited in excited states. This energy is dispersed by a miscellany of processes, of which the most important in pure rare gases is likely radiative decay. The nonlinear processes mentioned above both tend to reduce ϵ_c. In the absence of electron–electron collisions, the EEDF in typical discharges is generally Druyvesteyn-like, with a depleted high energy tail. Electron–electron collisions make the EEDF more Maxwellian, increasing the proportion of the discharge power that is deposited in high-threshold electron impact processes, so that the ionization rate increases at the expense of electronic excitation rates, thus reducing ϵ_c. Multi-step ionization processes compete with other decay processes for the energy deposited in excited states, so that some of this energy is recycled into ionization, and this also decreases ϵ_c.

3.2.2. Multistep ionization. Multistep ionization is examined in a simple theory retaining the assumption of a Maxwellian EEDF. In the simplest reasonable representation of the argon excited state manifold, the four lowest excited states are lumped into a single model state, Ar*, and all higher excited states are assumed to cascade collisionally or radiatively into this level. A more detailed model separating the metastable and resonance states of this composite level is discussed in the appendix. The loss processes for Ar* are electron impact ionization and radiative coupling to the ground state. Radiative decay of the composite state is at a rate which is a weighted average of the constituent states decay rates, each evaluated using the Holstein trapping factor [27]. This approximate treatment leads to an effective radiative lifetime which depends on the discharge dimensions and gas pressure, but which is likely to be in the range of 1–100 μs. Further discussion of the processes affecting the excited state densities can be found elsewhere [28–31]. With such a model for the excited state kinetics, there are two limiting cases: at low electron density, multistep ionization is not important, excited states decay radiatively and the excited state density increases linearly with electron density; at high electron density, radiative decay is not important, multistep ionization is the dominant loss process for excited states, and the excited state density is independent of electron density. The solution of a volume-averaged model including these kinetics shows that ϵ_{T_e} is considerably changed in passing from the first of these regimes to the second (figure 8). Moreover, the transition between these regimes occurs over the range of electron density that is typically crossed at the E-to-H transition of an inductive discharge. So these elementary calculations lead to an expectation of a substantial difference in ϵ_{T_e} between the inductive and capacitive modes.

More detailed calculations using the particle in cell approach mentioned above confirm these conclusions. A model system with cylindrical symmetry was investigated, having inner radius 2 cm and outer radius 6 cm, with the outer electrode grounded. The discharge is in argon at a pressure of 100 mTorr, with electron–neutral processes

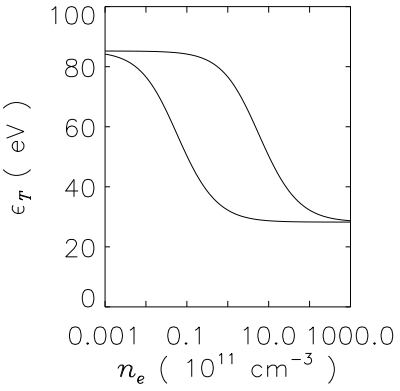

Figure 8. The total energy required per electron–ion pair, ϵ_T, as a function of electron density. The nonlinear behaviour shown here is produced by multistep ionization, as discussed in the text. The two curves are for different values of the effective radiative lifetime of excited states, τ = 1 ms (left-hand curve) and τ = 10 μs (right-hand curve). Note the effect saturates across the range of densities usually associated with the E-to-H transition.

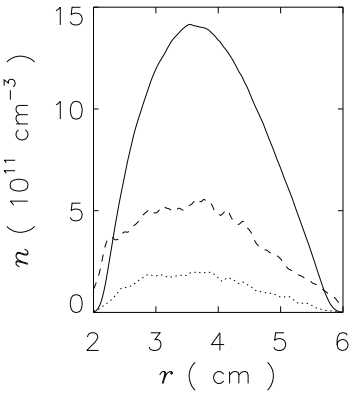

Figure 9. Species densities from a particle in cell simulation of an inductive discharge including excited states. The solid line shows the electron density (which is practically identical with the ion density), the dashed line is the Ar* density and the dotted line is the density of Ar**. These data are selected from the calculations summarized in figure 10, further details of which are discussed in the text.

using essentially the cross sections of [31], and ion–neutral processes using cross sections from [32] and [33]. This model can be excited either inductively or capacitively, by a boundary condition at the inner radial boundary forcing a current either radially (for capacitive excitation) or azimuthally (for inductive excitation). These calculations were aimed at verifying the results given above concerning the efficiency of plasma production in different operating regimes, and did not examine hysteresis effects directly. The treatment of the excited states adopted in the particle in cell calculations includes a second energy level, denoted as Ar** and representing essentially 6p states with an energy about 1.5 eV above the metastable levels. Appropriate additional collisional processes coupling the various states are also included. Representative plasma and excited state densities are shown in figure 9. Figure 10 shows the plasma density as a function of power absorbed by the discharge electrons for three cases: a capacitive discharge with no excited state kinetics; an inductive discharge with no excited state kinetics

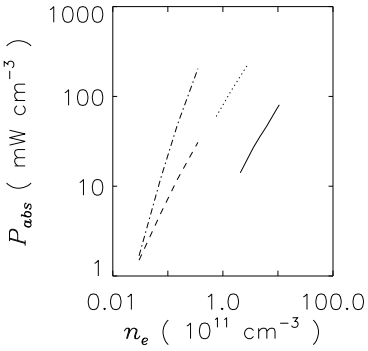

Figure 10. Particle in cell calculations showing volume averaged power density absorbed by the plasma from the circuit. The various curves show: (i) inductive mode with multistep ionization and Coulomb collisions (solid line); (ii) inductive mode without multistep ionization or Coulomb collisions (dotted line); (iii) power absorbed by electrons only in capacitive mode (dashed line) and (iv) total power absorbed by electrons and ions in capacitive mode (dot–dashed line). Note that curves (ii) and (iii) fall almost on the same straight line. These data are for a discharge in argon at a pressure of 100 mTorr, sustained between cylindrical electrodes of radii 2 and 6 cm.

and an inductive discharge including excited state kinetics and the electron–electron collisions to be discussed below. In the last of these cases we chose an improbably long radiative lifetime for the metastable state with the intention of demonstrating the effect of multistep ionization with maximum clarity. The results may however be taken as more representative for experiments where the area to volume ratio and/or the pressure are larger than our model system. It is evident that the ϵ_{T_e} calculated with respect to power deposited in electrons is almost the same for capacitive and inductive excitation when nonlinear effects are neglected. With respect to total power (which is what is normally measured in experiments), ϵ_T is of course much larger in capacitive mode, because substantial power is supplied to the ions.

3.2.3. Electron–electron collisions. Elaborate calculations are required to assess the importance of electron–electron collisions in detail, but simple estimates of their significance are available. We are chiefly interested in the effect on the high energy tail of the distribution function, which is depopulated by inelastic collisions of various kinds and losses at the plasma boundary. In steady state, this depopulation is replenished by a compensating flow of electrons from low energy to high energy, which is usually considered to be driven by the electric field only. When the density of electrons is large enough, however, there can be a significant contribution from electron–electron collisions. Comparison of the fluxes driven by Coulomb collisions and by the electric field shows that the former term will be larger at electron energy ϵ when [34]

$$\frac{n}{n_g} > \frac{e^2}{3m_e}\frac{(E_{eff}/n_g)^2}{\langle \nu_e/n_g\rangle}\frac{\sqrt{\epsilon}}{\alpha\sqrt{e/2\pi\epsilon_0 m_e}} \qquad (16)$$

where n_g is the neutral gas density, $E_{eff}^2 = (E^2/2)\nu_e^2/(\nu_e^2 + \omega^2)$ the effective electric field, with E the rf electric field amplitude, ν_e is the electron–neutral collision frequency,

and $\alpha = 2/3\pi(e^2/4\pi\epsilon_0)^2 \ln\Lambda$, with $\ln\Lambda$ the Coulomb logarithm. There are thus two crucial parameters to be considered in assessing the importance of electron–electron collisions: n/n_g and E_{eff}/n_g. The rf electric field amplitude E is not a very sensitive function either of discharge gas pressure or of rf power—typical values obtained in experiments [35, 36] are $\sim$1 V cm^{-1}—so E_{eff}/n_g normally decreases with increasing gas pressure and, for example, is likely to be around 10 Td (1 Td = 10^{-21} V m^{-2}) in argon at a pressure of 100 mTorr. It is commonly found that the plasma density that can be achieved in given conditions is such that n/n_g in the vicinity of the starting current is not a strong function of pressure, and this parameter can take values as large as 10^{-3} [22]. The inequality given by equation (16) then requires E_{eff}/n_g to be a few Td or less. It would appear then that electron–electron collisions cannot be a dominant effect at the lower end of the pressure range we are considering, but might become so at higher pressures. However, this issue is complicated by the assumption implicit in equation (16) of a uniform electric field. This is far from being the situation in an inductive discharge with the electromagnetic disturbance confined to a skin depth layer. At low pressure, when the nonlocal approximation [37] holds, the electric field in equation (16) might reasonably be replaced by an average over the plasma volume. At higher pressures, this is not appropriate and no simple approach is apparent. In either case the condition of equation (16) is unduly stringent, and electron–electron collisions might be more important that it suggests. We have not discussed the effect of electron–ion collisions, which at high enough plasma density and low enough gas pressure can affect the electron momentum transfer frequency [34]. Such conditions are not usual in inductive discharges of the class we are considering, but this is another potential source of hysteresis.

In the particle in cell calculations discussed above for an inductive discharge in argon at 100 mTorr, we find $E_{eff}/n_g \sim$ 40 Td, $n/n_g \sim 4 \times 10^{-4}$, and no significant parameter is changed by more than 5% by electron–electron collisions, which is consistent with the discussion above. However, the relatively large surface to volume ratio of this model system drives up the volume averaged electric field, which is often lower than this in experiments, as noted above.

In the global model to be discussed in section 4 we adopt a simple model for electron–electron collisions, with a transition from a Druyvesteyn to a Maxwellian EEDF near $n/n_g \approx 10^{-5}$ [34]. Here the Druyvesteyn and Maxwellian distributions are given by [38]

$$F_D \propto \mathcal{E}^{1/2}\, \mathrm{e}^{-0.547\mathcal{E}^2/\mathcal{E}_m^2} \tag{17}$$

$$F_M \propto \mathcal{E}^{1/2}\, \mathrm{e}^{-1.5\mathcal{E}/\mathcal{E}_m} \tag{18}$$

where $\mathcal{E}_m$ is the mean energy ($\mathcal{E}_m = 3T_e/2$ for a Maxwellian distribution). The mean energy is determined according to equation (1) by equating the production of pairs due to ionization to their loss to the walls:

$$K_{iz} n n_g \mathcal{V} = n u_B A_{eff} \tag{19}$$

where K_{iz} is the ionization rate constant, $\mathcal{V}$ is the plasma volume and $u_{BD} = (0.914e\mathcal{E}_m/M_g)^{1/2}$ and $u_{BM} = (0.667e\mathcal{E}_m/M_g)^{1/2}$ are the Bohm (ion loss) velocities at the sheath edge for the Druyvesteyn and Maxwellian distributions, respectively [38]. For a given pressure and discharge geometry, equation (19) determines $\mathcal{E}_m$. The collisional energy loss factor ϵ_c can then be evaluated by integrating the energy loss processes over the appropriate EEDF and summing the results. Applying this procedure, we find that the ratio of energy loss factors for argon at the same value of $\mathcal{E}_m$ (not the same pressure) is approximately

$$\frac{\epsilon_{cD}}{\epsilon_{cM}} \approx 1.27 + \frac{14.60}{\mathcal{E}_m} \tag{20}$$

over a range of $\mathcal{E}_m$ from 1 to 10 eV. Accounting for the transition from a Druyvesteyn to a Maxwellian distribution, we then adopt a heuristic form for the electron power loss:

$$P_{dis} \propto n\left(\frac{\epsilon_{cD}}{\epsilon_{cM}}\right)^{1/(1+10^5 n/n_g)} \tag{21}$$

where we have chosen the transition to occur at $n/n_g \approx 10^{-5}$.

3.2.4. Further remarks. The condition for multistep ionization in a weakly ionized diffusion-loss dominated discharge has the form [39] (see also the appendix)

$$n n_g > \text{const} \tag{22}$$

where n_g is the neutral gas density, while the condition for electron–electron collisions is given by equation (16) and has the same form if we assume that the electric field is approximately constant. (Measurements show that E, the induced electric field amplitude, is weakly dependent on both pressure and power [36]. Moreover, in the pressure range where hysteresis effects are most evident, $\nu_e > \omega$ so $E_{eff} \approx E/\sqrt{2}$.) Hence either process may dominate the other at low gas pressures, depending on the value of the constants in equation (22) (except in gases without metastable states at any pressures). At higher pressures, it will be apparent that if multistep ionization can dominate all other excited state decay processes, then electron–electron collisions must be of minor importance, since it does not matter how the electron energy is initially divided between excited states and one step ionization. The importance that these processes have at a given gas pressure depends on how large the electron density must become in order that they can be significant. Both of these processes are saturable nonlinearities that tend to produce curves of P_{dis} as a function of n_e with a kink, as in the example of figure 3. In this case there is a simple interpretation of the hysteresis effect in terms of equation (7). The transition from E to H mode is initiated from a low electron density, where ϵ_{T_e} is large, as at the left-hand side of figure 8. So the starting current must satisfy equation (7) with ϵ_{T_e} relatively large. On the other hand the H-to-E transition begins in a state with a relatively large electron density and correspondingly smaller ϵ_{T_e}. So the maintenance current need only satisfy equation (7) with this smaller value of ϵ_{T_e}.

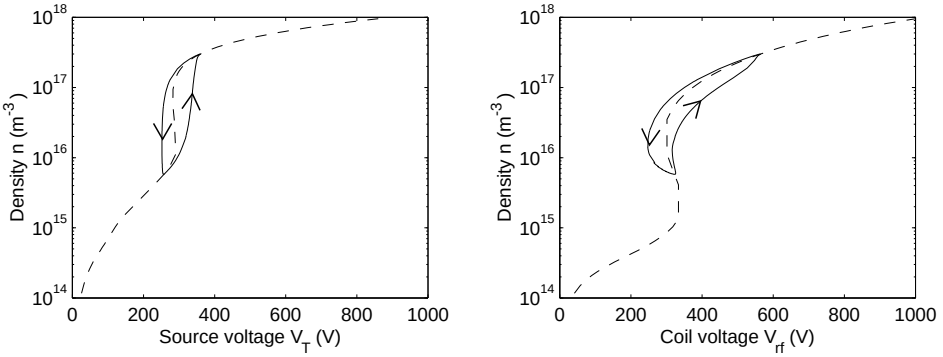

Figure 11. Density n versus antenna coil voltage V_{rf} and versus source voltage V_T at a pressure of 20 mTorr in argon; the dashed curves show the equilibrium, with the matching network elements set to match the discharge at the single point having $n = 3 \times 10^{17}$ m^{-3} ($P_{abs} = 1290$ W); the solid curves with arrows show the hysteresis loop generated for a $V_T(t)$ variation given in figure 12(a).

4. Global discharge model with hysteresis

In this section we discuss the interaction of the external circuit parameters—in particular the matching network—with the hysteresis mechanisms discussed above, which have been incorporated into a volume-averaged (global) argon discharge model, including the matching network shown in figure 4. This global model does not explicitly include multistep ionization, but as we have shown in section 3 above, for a fixed gas pressure the qualitative effect of multistep ionization is the same as that of electron–electron collisions: in both cases ϵ_{T_e} becomes a function of the electron density as shown in figure 8.

The high inductive voltage required for the antenna coil of an inductive discharge is generally supplied by a 50 Ω rf power source through a capacitive matching network [3], as shown in figure 4. Here C_s and C_p are variable series and parallel capacitors, and V_T and R_T (= 50 Ω) are the Thevenin-equivalent rf source voltage amplitude and resistance. As will be shown, the source resistance and matching network can significantly affect the hysteresis. In the global model, Kirchhoff's laws for the circuit of figure 4 are solved along with the particle and energy balance relations to determine the discharge equilibrium in the steady state for given settings of the matching network capacitors and for a specified source voltage V_T. This solution determines the density- and sheath-voltage-dependent element values in the circuit, the plasma parameters n and T_e and all voltages and currents. By choosing different values of V_T, the complete equilibrium characteristics can be determined.

The discharge response to a (slowly) time-varying rf source voltage amplitude $V_T(t)$ is then examined. This is done by solving the circuit equations along with the differential equations for particle and energy conservation. A typical voltage variation chosen is

$$V_T(t) = V_{T0} - \frac{\Delta V_{T0}}{2}(1 - \cos \omega_{slow} t). \qquad (23)$$

Different types of hysteresis curve can be examined depending on the values V_{T0}, ΔV_{T0} and ω_{slow} that are chosen.

Figure 11 shows the equilibrium (dashed) curves of density n versus source voltage V_T and n versus antenna coil voltage V_{rf} for an inductive discharge driven by a three-turn coil (resistance 0.1 Ω) at 13.56 MHz, and incorporating as a hysteresis mechanism the rearrangement of the EEDF from a Druyvesteyn distribution at low densities to a Maxwellian distribution at high densities, according to equation (21). The discharge is modelled as a cylinder of height 7.5 cm and radius 10.25 cm. The argon pressure is 20 mTorr and a quartz window thickness of 1 cm is used. The matching network capacitors C_s and C_p were chosen to match the source to the load at a single value of $V_T = 360$ V, corresponding to the single density $n = 3 \times 10^{17}$ m^{-3} and absorbed power $P_{abs} = 1290$ W, well within the H mode. It is apparent from the equilibrium curves that the discharge is in H mode for $n > 10^{17}$ m^{-3} and in E mode for $n < 10^{16}$ m^{-3}. The curves bend back on themselves in the range $V_T \sim$ 270–290 V, indicating the presence of hysteresis. Figure 11 also shows the hysteresis loop (solid curves with arrows) generated by a $V_T(t)$ variation with $\Delta V_{T0} = 0.3 V_{T0}$ and $T_{slow} = 2\pi/\omega_{slow} = 5$ ms. The time-varying source voltage is shown in figure 12, along with the resulting variation in the density and the sheath voltage. It is seen from the density and sheath voltage time variation that the discharge cycles between H and E modes. In contrast, for $\Delta V_{T0} = 0.2 V_{T0}$, the discharge is found to always remain in H mode, and the time variation merely traces out the equilibrium characteristics.

We have found that the region of source voltages over which the density bends back on itself (region of hysteresis) decreases with increasing pressure. For example, at 40 mTorr the same initial density $n = 3 \times 10^{17}$ m^{-3} ($V_T = 334$ V, $P_{abs} = 1120$ W) lies considerably above the region of hysteresis ($V_T \sim$ 210–230 V). Hence, a larger reduction in V_T ($\Delta V_{T0} \approx 0.4 V_{T0}$) is required to cycle between H and E modes. We have also noted that the range of source voltages over which the density bends back on itself increases with decreasing frequency. However, a detailed parametric study of the dependence on pressure and frequency has not been performed.

It is noteworthy that the hysteresis loop is determined by the density–source voltage characteristics, and not by the density–antenna coil voltage characteristics. This is evident from figure 11, where the backward (negative slope) part of the density–antenna coil voltage characteristics is accessed during the motion around the hysteresis loop. This demonstrates the importance of the source resistance and matching network impedance in modifying the hysteresis characteristics.

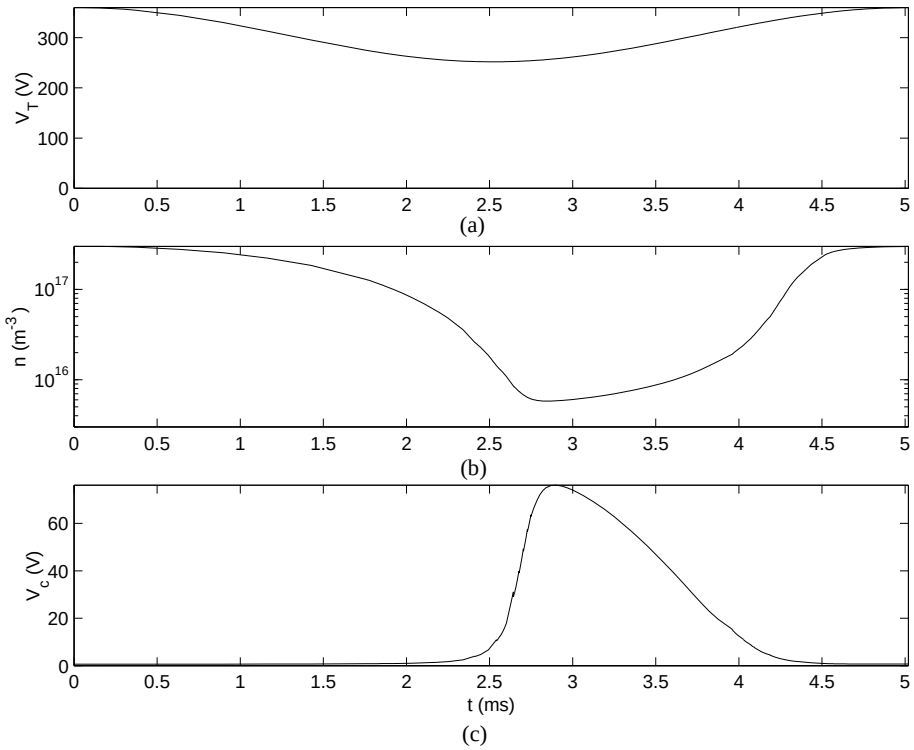

Figure 12. Source voltage amplitude V_T (a), sheath edge density n (b) and sheath voltage V_c (c) versus time for the hysteresis loop shown in figure 11.

5. Conclusion

We have shown that in general the origin of hysteresis effects in inductive discharges must be sought in the electron power balance equation. When this equation has multiple solutions for a given value of the coil current—as shown in figure 3—hysteresis will appear. There will then be a range of values of the coil current that permit either E or H mode discharges to exist, and there will be discontinuous jumps in operating parameters between the modes. Effects of this type are observed in experiments, and can be large: the ratio of the starting current for the H mode to the minimum maintenance current can be as much as a factor of three [12]. Although hysteresis on this scale may not be common, a degree of hysteresis is probably ubiquitous.

We have attempted to catalogue the mechanisms that produce hysteresis. These mechanisms can be conveniently divided into circuit mechanisms affecting the rate of power absorption by the discharge, and plasma mechanisms affecting the efficiency of conversion of power into ionization. Each of these groups of mechanisms affects the electron power balance differently: circuit nonlinearities appear on the left-hand side of the power balance equation, equation (7), while plasma nonlinearities appear on the right-hand side. Moreover, since the circuit mechanisms we have identified all involve the capacitive coupling, these two classes of nonlinearities may in principle be distinguished experimentally with the help of a Faraday shield, although no such experiments are known to us.

It is difficult to be categorical about the relative importance in practice of the various mechanisms we have described, in part because of the limited experimental data presently in hand, and in part because of the large parameter space in which inductive discharges are operated: the answers are probably not the same in every case. Some general remarks are possible however. Electron–electron collisions are evidently a universal phenomenon, in that they are present in all discharges, but this is a difficult effect to evaluate precisely in the general case, short of a large-scale kinetic calculation which would necessarily be numerical. Multistep ionization can be important in the smaller but still significant class of discharges where the chemistry supports long-lived excited states. Again, detailed evaluation is difficult without precise knowledge of the excited state kinetics. The circuit-side effects are also universal, in that they will appear in any inductive discharge without an ideal Faraday shield. We should note that, as far as we can determine, the presence of hysteresis does not lead to instabilities in electropositive gases. In particular, the H mode is stable with respect to the E mode even when both are allowed at a given coil current. A full quantitative understanding of all these effects will require more detailed experiments and improved models.

Appendix. Multistep ionization

We consider a simple model for multistep ionization in a low pressure discharge [39]. Let ϵ_{0i} and ϵ_{mi} be the ionization energies from the ground and metastable levels, having degeneracies g_0 and g_m and densities n_0 and n_m, respectively. In the steady state we have

$$\frac{\mathrm{d}n_m}{\mathrm{d}t} = k_{0m} n_e n_0 - k_{m0} n_e n_m - \frac{n_m}{\tau_m} = 0 \qquad \text{(A1)}$$

where n_e is the electron density, k_{0m} is the forward rate constant for excitation of the metastable levels from the ground state, k_{m0} is the corresponding rate for (superelastic) de-excitation of metastable levels and τ_m is the characteristic time for loss of excited species to the walls. From the detailed balance condition, we find

$$k_{0m} = k_{m0}\frac{g_m}{g_0}\exp(-(\epsilon_{0i} - \epsilon_{mi})/k_B T_e). \tag{A2}$$

Substituting equation (A2) into (A1) we find

$$n_m = n_0\frac{g_m}{g_0}\exp(-(\epsilon_{0i} - \epsilon_{mi})/k_B T_e)\frac{1}{(1 + n_e k_{m0}\tau_m)^{-1}}. \tag{A3}$$

The ratio of the ionization rates ν_{0i} and ν_{mi} from the ground and metastable levels is

$$\frac{\nu_{0i}}{\nu_{mi}} \approx \frac{n_0\exp(-\epsilon_{0i}/k_B T_e)}{n_m\exp(-\epsilon_{mi}/k_B T_e)}\left(\frac{\epsilon_{mi}}{\epsilon_{0i}}\right)^2. \tag{A4}$$

Substituting (A4) into (A3) yields the condition for multistep ionization

$$n_e k_{m0}\tau_m\frac{g_m}{g_0} > \left(\frac{\epsilon_{mi}}{\epsilon_{0i}}\right)^2. \tag{A5}$$

For a diffusive loss of metastables to the walls

$$\tau_m = \frac{\Lambda^2}{D_m} \tag{A6}$$

where D_m is the metastable diffusion coefficient and Λ is the characteristic size of the discharge. Because $D_m \propto n_g^{-1}$, equation (A5) has the form

$$n_e n_g > \text{const.} \tag{A7}$$

For argon, the energies of the metastable and resonance levels practically coincide, and electron collisional transfer between the metastable and resonance levels occurs with a large rate coefficient, k_{mr}. Assuming that the resonance level density is small and neglecting metastable loss by de-excitation and by diffusion to the walls, equation (A1) is modified to

$$\frac{\mathrm{d}n_m}{\mathrm{d}t} = k_{0m} n_e n_0 - k_{mr} n_e n_m. \tag{A8}$$

Solving equation (A8) for n_m and using equation (A2), we obtain

$$n_m = n_0\frac{g_m}{g_0}\frac{k_{m0}}{k_{mr}}\exp(-(\epsilon_{0i} - \epsilon_{mi})/k_B T_e). \tag{A9}$$

Substituting equation (A9) into equation (A4), we find

$$\frac{\nu_{0i}}{\nu_{mi}} \approx \frac{g_0}{g_m}\frac{k_{mr}}{k_{m0}}\left(\frac{\epsilon_{mi}}{\epsilon_{0i}}\right)^2. \tag{A10}$$

For an argon discharge with $T_e = 3$ eV, we have [30] $g_0 = 1$, $g_m = 6$, $k_{mr} \approx 2 \times 10^{-7}$ cm^3 s^{-1} and $k_{m0} \approx 5 \times 10^{-10}$ cm^3 s^{-1}, yielding

$$\frac{\nu_{0i}}{\nu_{mi}} \sim 5 \tag{A11}$$

hence the condition for multi-step ionization is not obtained.

However, re-absorption of optical emission from the resonance level by ground state atoms can lead to a resonance level density of order of the metastable level density. In this case the reverse electron collisional transfer process, from resonance to metastable levels, becomes important in equation (A8), and the condition for multistep ionization can be met. The effective radiative decay rate from the resonance levels can be written as

$$A_{eff} = A_{21}\frac{S}{V}\frac{1}{n_g\sigma_\nu} \tag{A12}$$

where A_{21} is the Einstein A coefficient, S/V is the surface to volume ratio of the discharge and σ_ν is the optical absorption cross section. Evaluating equation (A12) for a typical discharge size ($S/V \approx 0.4$ cm^{-1}) we obtain $A_{eff} \approx 2.5 \times 10^{21}/n_g$ s^{-1}, with n_g in cm^{-3}. The ratio of resonance to metastable densities may be estimated as

$$\frac{n_r}{n_m} \approx \frac{k_{mr} n_e}{A_{eff}} \sim 0.8 \times 10^{-28} n_e n_g \tag{A13}$$

hence the condition for multistep ionization in argon is $n_e n_g > 1.2 \times 10^{28}$ cm^{-6}.

Acknowledgments

This work was partially supported by National Science Foundation Grant ECS-9202993; EURATOM, via grants to the Irish Fusion Association; a gift from the Lam Research Corporation and the University of California Semiconductor Manufacturing Alliance for Research and Training. The authors are also indebted to Professor M J Kushner, who made available certain cross sections used in the particle in cell calculations.

References

[1] Eckert H U 1986 *2nd Ann. Conf. on Plasma Chemistry and Technology* ed H V Boenig (Lancaster, PA: Technomic) pp 171–202
[2] Graves D B 1994 *IEEE Trans. Plasma Sci.* **22** 31
[3] Lieberman M A and Lichtenberg A J 1994 *Principles of Plasma Discharges and Materials Processing* (New York: Wiley)
[4] Keller J H 1996 *Plasma Sources Sci. Technol.* **5** 166
[5] Thompson J J 1927 *Phil. Mag.* **4** 1128
[6] Townsend J S and Donaldson R H 1928 *Phil. Mag.* **5** 179
[7] MacKinnon K A *Phil. Mag.* **8** 605
[8] Knipp C T 1931 *Phys. Rev.* **37** 756
[9] Kortshagen U, Gibson N D and Lawler J E 1996 *J. Phys. D: Appl. Phys.* **29** 1224
[10] Suzuki K, Nakamura K, Ohkubo H and Sugai H 1998 *Plasma Sources Sci. Technol.* **7** 13
[11] Yoon N S, Kim B C, Yang J G and Hwang S M 1998 *IEEE Trans. Plasma Sci.* **26** 190
[12] El-Fayoumi I M, Jones I R and Turner M M 1998 *J. Phys. D: Appl. Phys.* **31** 3082
[13] Smith H, Lynch W A and Hilberry N 1931 *Phys. Rev.* **37** 1091
[14] Franklin R N 1976 *Plasma Phenomena in Gas Discharges* (Oxford: Clarendon)
[15] Turner M M 1993 *Phys. Rev. Lett.* **71** 1844
[16] Turner M M 1996 *Plasma Sources Sci. Technol.* **5** 159
[17] Birdsall C K and Langdon A B 1985 *Plasma Physics via Computer Simulation* (New York: McGraw-Hill)

[18] Birdsall C K 1991 *IEEE Trans. Plasma Sci.* **19** 65
[19] Hewett D and Langdon A B 1987 *J. Comput. Phys.* **72** 121
[20] Nanbu K 1997 *Phys. Rev.* E **55** 4642
[21] Piejak R B, Godyak V A and Alexandrovich B M 1992 *Plasma Sources Sci. Technol.* **1** 179
[22] Keller J H, Forster J C and Barnes M S 1993 *J. Vac. Sci. Technol.* A **11** 2487
[23] Godyak V A and Khanneh A S 1986 *IEEE Trans. Plasma Sci.* **14** 112
[24] Raizer V P, Shneider M N and Yatsenko N A 1995 *Radio-Frequency Capacitive Discharges* (Boca Raton, FL: Chemical Rubber Company)
[25] Lieberman M A and Boswell R W 1998 *J. Physique* IV **8** 145
[26] Forrest J R and Franklin R N 1969 *J. Phys. B: At. Mol. Opt. Phys.* **2** 471
[27] Holstein T 1951 *Phys. Rev.* **83** 1159
[28] Scheller G R, Gottscho R A, Graves D B and Intrator T 1988 *J. Appl. Phys.* **64** 598
[29] McMillin B K and Zachariah M R 1995 *J. Appl. Phys.* **77** 5538
[30] Ashida S, Lee C and Lieberman M A 1995 *J. Vac. Sci. Technol.* A **13** 2498
[31] Rauf S and Kushner M J 1997 *J. Appl. Phys.* **82** 2805
[32] Phelps A V 1991 *J. Chem. Phys. Ref. Data* **20** 557
[33] Phelps A V 1994 *J. Appl. Phys.* **76** 747
[34] Rockwood S D 1974 *J. Appl. Phys.* **45** 5229
[35] Hopwood J, Guanieri C R, Whitehair S J and Cuomo J J 1993 *J. Vac. Sci. Technol.* A **11** 147
[36] Piejak R, Godyak V and Alexandrovich B 1995 *J. Appl. Phys.* **79** 5296
[37] Kortshagen U, Busch C and Tsendin L D 1996 *Plasma Sources Sci. Technol.* **5** 1
[38] Amemiya H 1997 *J. Phys. Soc. Japan* **66** 1335
[39] Smirnov B M 1981 *Physics of Weakly Ionized Gases* (Moscow: Mir)